



HAL
open science

Multimodal Plasmonic Hybrids: Efficient and Selective Photocatalysts

Yoel Negrín-Montecelo, Xiang-Tian Kong, Lucas V Besteiro, Enrique Carbo-Argibay, Zhiming M Wang, Moisés Pérez-Lorenzo, Alexander O Govorov, Miguel Comesaña-Hermo, Miguel A Correa-Duarte

► **To cite this version:**

Yoel Negrín-Montecelo, Xiang-Tian Kong, Lucas V Besteiro, Enrique Carbo-Argibay, Zhiming M Wang, et al.. Multimodal Plasmonic Hybrids: Efficient and Selective Photocatalysts. 2021. hal-03430903v1

HAL Id: hal-03430903

<https://hal.science/hal-03430903v1>

Preprint submitted on 16 Nov 2021 (v1), last revised 24 Jan 2022 (v2)

HAL is a multi-disciplinary open access archive for the deposit and dissemination of scientific research documents, whether they are published or not. The documents may come from teaching and research institutions in France or abroad, or from public or private research centers.

L'archive ouverte pluridisciplinaire **HAL**, est destinée au dépôt et à la diffusion de documents scientifiques de niveau recherche, publiés ou non, émanant des établissements d'enseignement et de recherche français ou étrangers, des laboratoires publics ou privés.

Multimodal Plasmonic Hybrids: Efficient and Selective Photocatalysts

Yoel Negrín-Montecelo,^{1,2} Xiang-Tian Kong,^{3,4} Lucas V. Besteiro,^{1,2} Enrique Carbó-Argibay,⁵ Zhiming M. Wang,⁴ Moisés Pérez-Lorenzo,^{1,2} Alexander O. Govorov,^{3,*} Miguel Comesaña-Hermo^{6,*} and Miguel A. Correa-Duarte^{1,2,*}

¹CINBIO, Universidade de Vigo, Department of Physical Chemistry, 36310 Vigo, Spain

²Galicia Sur Health Research Institute (IISGS), CIBERSAM, 36310 Vigo, Spain

³Department of Physics and Astronomy, Ohio University, Athens, Ohio 45701, United States

⁴Institute of Fundamental and Frontier Sciences, University of Electronic Science and Technology of China, Chengdu, 610054, China

⁵International Iberian Nanotechnology Laboratory, Av. Mestre José Veiga s/n, 4715-330 Braga, Portugal

⁶Université de Paris, ITODYS, CNRS, UMR 7086, 15 rue J-A de Baïf, F-75013 Paris, France

govorov@ohiou.edu, miguel.comesana-hermo@u-paris.fr, macorrea@uvigo.es

Abstract: Important efforts are currently under way in order to implement plasmonic phenomena in the growing field of photocatalysis, striving for improved efficiency and reaction selectivity. A significant fraction of such efforts have been focused on distinguishing, understanding and enhancing specific energy transfer mechanisms from plasmonic nanostructures to their environment. Herein we report a synthetic strategy that brings together two of the main physical mechanisms driving plasmonic photocatalysis into an engineered system by rationally combining the photochemical features of energetic charge carriers and the electromagnetic field enhancement inherent to the plasmonic excitation. We do so by creating hybrid photocatalysts that integrate multiple plasmonic resonators in a single entity, controlling their joint contribution through spectral separation and differential surface functionalization. This strategy allows us to study the combination of different photosensitization mechanisms when activated simultaneously. Our results show that hot electron injection can be combined with an energy transfer process mediated by near-field interaction, leading to a significant increase of the final photocatalytic response of the material. In this manner, we overcome the limitations that hinder photocatalysis driven only by a single energy transfer mechanism, and move the field of plasmonic photocatalysis closer to energy-efficient applications. Furthermore, our

multimodal hybrids offer a test system to probe the properties of the two targeted mechanisms and open the door to wavelength-selective photocatalysis and novel tandem reactions.

Introduction:

In the last decades, plasmonic metal nanoparticles (NPs) have gained relevance as photosensitizers given their ability to extend the photocatalytic efficiency of large bandgap semiconductors, such as TiO₂, to a broader range of the electromagnetic spectrum. As a result, metal-semiconductor nanoarchitectures have been promoted to the forefront of the rapidly developing fields of photovoltaics, photochemistry and photoelectrochemistry.¹⁻⁶ Along these lines, these hybrid nanosystems can be exploited in order to increase the overall performance of solar cells,⁷⁻⁹ drive different organic transformations,^{10,11} or boost water splitting efficiency.^{12,13}

Plasmonic photosensitization of semiconductors results from the ability of metal NPs to support collective electronic oscillations, also known as localized surface plasmon resonances (LSPRs), excited upon light irradiation. The plasmonic excitations of coinage metals (Ag, Au, Cu) are strong, narrow, and highly tunable through changes in the geometry of the NPs, leading to absorption signatures with high versatility that span through the visible and near-infrared (NIR) regions of the electromagnetic spectrum.¹⁴ Moreover, LSPRs confer these metallic objects with very high absorption cross-sections¹⁵ and the ability to behave as light concentrators by holding strong electromagnetic field enhancements at their surfaces, features that render them ideal candidates in sensing and theranostic applications.¹⁶ Once excited, plasmonic resonances can transfer their energy to a nearby acceptor thanks to the ability of metal NPs to create a population of excited “hot charge carriers” upon visible and/or NIR irradiation.¹⁷⁻²¹ The term “hot charge carriers” describes the non-thermal distribution of electrons and holes created upon optical excitation of a plasmonic resonator. Even though they are short-lived in nature (< 100 fs), under continuous wave (CW) illumination they are being constantly excited, hence ensuring the formation of a steady-state population. Interestingly, hot carriers can be injected through the Schottky barrier created at a metal-semiconductor interface, avoiding relaxation through thermalization processes.^{22,23} This effect, known as hot electron injection (HEI), allows the electrons to propagate to the conduction band of the semiconductor, leading to a privileged catalytic site for reduction reactions, while the holes created below the Fermi level of the metal can be used to drive oxidation reactions.²⁴

It is generally accepted that a correct band alignment and the formation of a physical interface between the metal and the semiconductor are essential parameters in order to obtain an efficient HEI process.²⁵ However,

the use of plasmonic hot electrons as a powerful means to photosensitize large bandgap semiconductors faces important limitations. Firstly, plasmonic excitations are mostly composed of low energy electronic states, hence leading to a majority of charges not having sufficient energy to overcome the Schottky barrier.²⁶ Accordingly, the number of hot electrons that can be extracted from a given plasmonic resonator is intrinsically limited. Moreover, even in those scenarios in which an efficient HEI across the Schottky barrier can be attained, another limitation related to the metal concentration is observed. Along these lines, when exceeding a certain metal concentration threshold, a further rise in the amount of photosensitizer induces a decrease in the photocatalytic efficiency. Previous reports explain this effect as a consequence of the electron-hole pair recombination under specific metal concentrations.²⁷⁻²⁹ In this case, metal components behave as recombination centers, providing an additional decay channel for the excited carriers in the semiconductor, reducing substantially the lifetime of the electron-hole pairs that contribute to the overall photocatalytic activity.

Plasmonic photosensitization can be also achieved through mechanisms not involving a charge transfer between the different components. In fact, the electromagnetic field enhancement associated to a given plasmonic excitation can drive an enhanced photosensitization of a nearby acceptor such as a large bandgap semiconductor.²⁵ The nature of this interaction, which will be referred to as plasmon-induced energy transfer (PET), is generally associated with the ability of plasmonic NPs to focalize the incoming photons onto their immediate surfaces, hence increasing the local photonic density of states and as a result, the effective absorption cross-section of the acceptor.³⁰ Other works discuss this interaction in terms of a dipole-dipole coupling established between the absorption signature of the plasmonic resonator and the excitation band of the semiconductor, leading to the non-radiative excitation of the latter.^{31,32} In contrast to HEI, PET processes can be active in geometries in which the plasmonic sensitizer and the semiconductor are separated by an insulating material. The optimum thickness of such insulator remains a source of discussion: while some works claim that the near-field effect becomes insignificant beyond 3 nm,³⁰ others alternatively point out to an optimum distance of 10 nm by asserting that shorter distances may increase back-energy transfer from the semiconductor to the metal NP.²⁵ Attending to the physical description of the PET effect, this optimal thickness should depend on different characteristics of the system. Among those, the strength and spatial extension of

the near-field enhancement of the resonator are likely to be relevant factors given their sensitivity to the geometrical features of the NP, such as the surface curvature.

Different examples in the literature show that the photocatalytic activity of plasmonic NPs can be driven by thermal effects, hot charges or the electromagnetic field enhancement; depending on the chemical reaction under study, the chemical composition and morphology of the resonator and the illumination conditions.^{33–35}

Moreover, the plasmonic photosensitization of a large bandgap semiconductor depends strongly on the surface functionalization of the metal and the relative disposition of the different materials forming the hybrid.^{28,36,37}

Along these lines, the rational design of a composite material in which the relative importance of HEI and PET mechanisms could be carefully monitored, would represent a relevant accomplishment.³⁸ Pre-designed

cooperative effects between different mechanisms can allow for a more efficient photosensitization in systems currently suffering from the limitations inherent to each mechanism when operating independently. Among

the few reports tackling this issue, Cushing and coworkers have developed a hybrid architecture in which HEI and PET mechanisms coexist.³⁹ In this work, when both photosensitization mechanisms are allowed by the

geometry of the system and the nature of the materials involved, the latter is found to be responsible for the majority of the photocatalytic activation of the semiconductor. The authors explain this result in terms of

transfer efficiency: the near field effect efficiency being very similar to that of the direct excitation of the semiconductor while that of charge transfer is usually limited (*vide supra*). In a different work, You and

coworkers reach similar conclusions when developing a theoretical model to characterize the relative importance of HEI and PET.⁴⁰ The authors find that HEI exhibits a low efficiency as a result of the energy

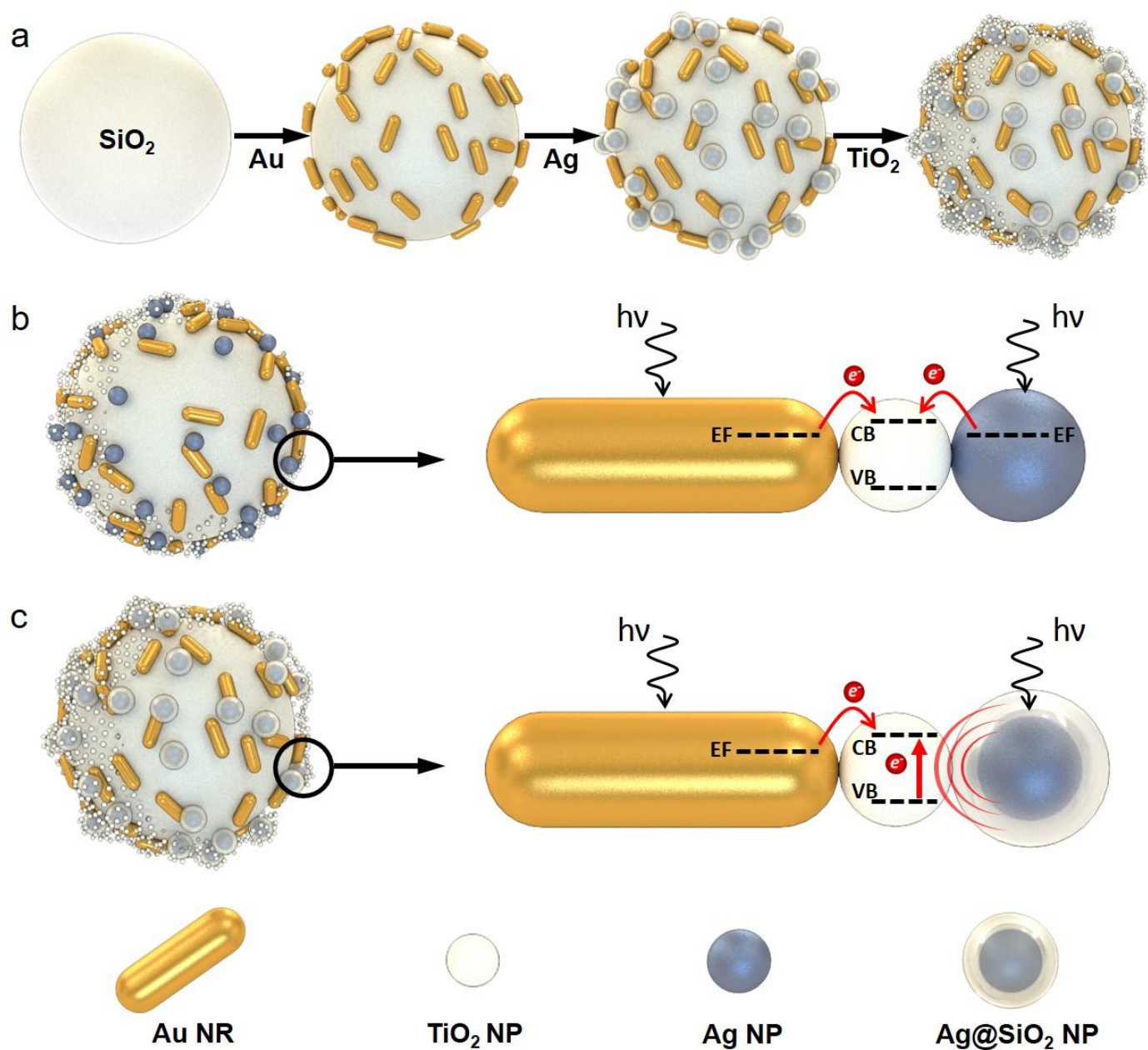
distribution of the hot electrons on the plasmonic metal. Even though these examples can work as a generic compass allowing the prediction of the relative importance of both processes in some systems, important

issues concerning the cooperative integration of different photosensitization mechanisms and their combination towards the development of a hybrid photocatalyst with improved performances have yet to be

addressed.

In this work we provide new insights into HEI and PET mechanisms when participating simultaneously in the photosensitization of a large bandgap semiconductor. With this aim, we present a new class of metal-semiconductor hybrids in which two different types of plasmonic resonators coexist. In this way the unique

cooperative interactions found in these superstructures (Scheme 1) can be rationally predicted and engineered. Along these lines, the photocatalytic activity of a system in which HEI has reached its maximum photosensitization capacity can be enhanced by the controlled integration of a PET-operated pathway, moving this technology towards energy-efficient applications. Moreover, the combination of plasmonic resonators with well-differentiated signatures can lead to multimodal hybrids with wavelength-selective photosensitization capabilities, opening the door to more advanced features such as photocatalytic tandem reactions.



Scheme 1. (a) Representation of the different steps of the assembly process used for the formation of the hybrid photocatalysts containing two different plasmonic resonators and TiO₂ NPs. (b) Hybrid system

composed by the combination of Au NRs and Ag NPs, being HEI the main photosensitization mechanism for both materials. (c) Hybrid system composed by the combination of Au NRs and Ag NPs coated with a SiO₂ shell, being HEI and PET the key operating mechanisms, respectively.

Results and discussion:

As previously mentioned, the physicochemical properties of a plasmonic object are particularly important to understand its interaction with a given semiconductor. Along these lines, the composition, morphology, size and surface functionalization of the metal will dictate the dominant photosensitization mechanism of the hybrid obtained and its overall efficiency.^{28,37} For this reason, three types of plasmonic NPs have been synthesized in order to fabricate the hybrid metal-semiconductor nanostructures reported herein. In this way, the different interactions between the metal and the semiconductor and thus, the distinctive photosensitization mechanisms established in these architectures, may be assessed separately (Figure 1a-c and S1). Accordingly, two plasmonic resonators showing a dominant HEI-based photosensitization have been selected: (i) Au nanorods (NRs) with an aspect ratio of 4 (53.8 nm x 13.3 nm) and a longitudinal plasmon band centered at 818 nm in water and (ii) spherical Ag NPs with a 42 nm diameter displaying a plasmonic signature centered at 417 nm in water. For the PET-based mechanism, Ag NPs functionalized with a 10 nm SiO₂ layer (Ag@SiO₂ NPs) and showing a plasmon signature red-shifted to 436 nm have been selected.

In order to develop a model platform in which the interaction between the different components can be easily controlled and analyzed, we have made use of the layer-by-layer assembly protocol.⁴¹ SiO₂ particles with a 500 nm diameter have been used as colloidal substrates, providing a homogeneous interface for the assembly of the plasmonic objects and the semiconductor (TiO₂ NPs) (Scheme 1).²⁸ More precisely, a first layer of the chosen plasmonic entity is deposited through electrostatic interactions, while a second layer of 5 nm TiO₂ (anatase phase) NPs is adsorbed in a subsequent step (see Supporting Information for details). Importantly, the hybrids formed in this way present high colloidal stability and are easily recoverable from the reaction medium by simple centrifugation.

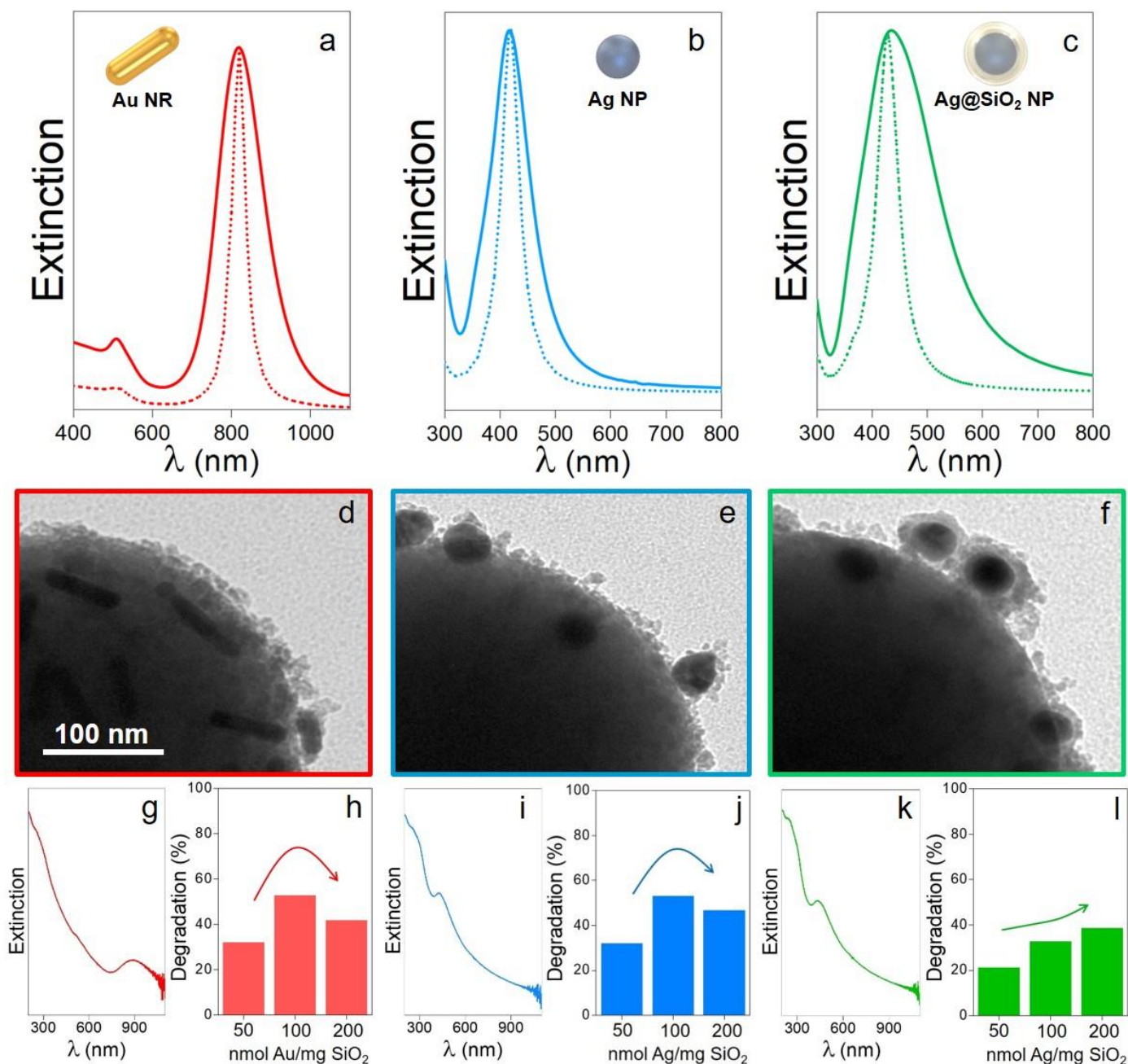


Figure 1. (a-c) Experimental (solid) and theoretical (dotted) extinction spectra of the different plasmonic NPs used as photosensitizers: Au NRs (red), Ag NPs (blue) and Ag@SiO₂ NPs (green). (d-l) TEM images, extinction spectra and photocatalytic degradation activities (with different metal/TiO₂ ratios) of the nanohybrids formed with Au NRs (red), Ag NPs (blue) and Ag@SiO₂ NPs (green).

Figure 1d-f and Figure S2 show TEM images of the hybrids obtained from the three different plasmonic entities. In all cases we can observe the formation of a smooth layer of TiO₂ NPs covering the entire surface of the composite, thus ensuring a good contact between the photosensitizer and the semiconductor. Interestingly, the extinction spectra of each nanohybrid shows an important scattering contribution coming

from the colloidal SiO₂ particles that hides the excitation band of TiO₂. Nevertheless, the plasmonic signature of each metal NP is easily discernible (Figure 1g, i, k). The redshift of the main plasmonic signatures with respect to the original plasmon band of the metal NPs in aqueous solution can be ascribed to the modification of the refractive index when adsorbed onto the SiO₂ spheres and coated with a thin layer of TiO₂ NPs (Figure S3).

In order to ascertain the photocatalytic features of the different hybrids, we have used the photo-transformation of rhodamine B (RhB) in aqueous solutions as a model reaction. This fluorescent probe can be transformed into the non-fluorescent rhodamine 110 through the action of reactive oxygen species (ROS) such as the hydroxyl and superoxide radicals that are generated after the interaction between the hot carriers (both electrons and holes) and water/oxygen molecules.⁴² In this way, the photodegradation of the organic dye can be quantified by following the decrease in absorbance (% of degradation) as a function of irradiation time. With this purpose, a solar simulator has been used as a light source, having an irradiation spectrum that covers the region between 350 and 2400 nm. Moreover, the photocatalytic experiments are performed at 298 K, using a jacketed reactor in order to minimize any possible thermal contributions. Along these lines, disentanglement between thermal processes and carrier-induced catalysis is a major point to take into consideration when considering plasmon-induced photocatalysis.^{19,43-45} As a control experiment, the photocatalytic activity of SiO₂ spheres functionalized solely with TiO₂ NPs has been tested (Figure S4). These objects present a reduced degradation of RhB after 180 min of irradiation (12%) that comes from the direct activation of TiO₂ with the UV irradiation of the solar simulator. The same photocatalytic reaction in the presence of SiO₂ spheres functionalized only with Au NRs leads to no degradation (Figure S4), evidencing that heat dissipation through plasmonic excitation alone cannot explain the photo-transformation of the probe. This result also demonstrates the absence of direct injection of carriers from the metal to the molecular species.

We have verified the optimal amount of metal component needed for a maximum photosensitization of the semiconductor. To this end, the amount of photosensitizer has been adjusted while keeping constant the remaining parameters (i.e. same amount of TiO₂ and SiO₂ support). The photodegradation of RhB after 180 min of irradiation is presented in Figure 1h, j and l for hybrids containing Au NRs, Ag NPs and Ag@SiO₂ NPs, respectively (the photocatalytic profiles are presented in Figure S5). Along these lines, the two

nanohybrids in which the plasmonic element forms a Schottky barrier with the semiconductor (Au NRs and naked Ag NPs) present an increase in the catalytic activity until a maximum level is reached (100 nmol of metal/mg SiO₂), leading in both cases to a degradation of 53% (Figure 1h, j). Above this concentration, a partial loss in activity is observed. As previously stated, such effect can be ascribed to the role played by the metal NPs as recombination centers, acting as acceptors for excited charge carriers in the semiconductor, and thus leading to the faster annihilation of the electron-hole pair in a HEI process. Interestingly, only the hybrid in which HEI can be ruled out due to the insulating layer between the plasmonic NP and the semiconductor (Ag@SiO₂ NPs) presents an increase in the catalytic activity above that critical threshold, which is consistent with a PET process (Figure 1l).

The HEI and PET mechanisms can be modeled in terms of the hot electron generation rate (which serves as a proxy of the injection rates) and the electromagnetic field enhancement for each plasmonic resonator. As shown in previous works, the excitation of plasmonic bands creates the conditions for the excitation of large numbers of hot carriers in the metal NPs (Figure 2a). As mentioned above, these excited hot carriers differ from those participating in the collective plasmonic wave in that they have larger energies, up to the total energy of the incoming photons. This can occur due to the interaction of electrons and holes with the metal phonons⁴⁶ and, importantly, the surface of the NPs.⁴⁷ The rates of generation of such intraband hot carriers can be subdivided in two different components, according to whether they have enough energy to surpass the Schottky barrier separating the metal and semiconductor, with a height of ~1 eV in our case.^{48,49} The comparison of the hot carrier generation rates between Au NRs and Ag NPs in Figure 2a showcases again their spectral differences, and also identifies the Ag NPs as the better resonator for exciting the larger numbers of hot carriers. This contrast arises from the difference of material composition and the averaging of the strong longitudinal plasmonic mode of the Au NR with its significantly weaker transversal mode.²⁶ On the other hand, Au NRs provide a stronger electromagnetic field enhancement around them,²⁸ as quantified by averaging this magnitude in the volume immediately surrounding them (Figure 2b). This is caused by their strong and spatially extended main dipolar mode (see Figure S3d).

Ag NPs also present a high density of hot charges and an electromagnetic field enhancement that coincide with the plasmonic signature of these objects (Figure 2a, b). In opposition to Au NRs, the latter effect appears

in the vicinity of the absorption wavelengths of TiO₂, implying that both effects (HEI and PET) can participate in the photoactivation mechanism. Although the average field enhancement outside of the Ag NP is significantly smaller than that of the Au NR due to the weaker dipolar moment of its plasmon, it is sufficient to achieve an effective enhancement above 1 order of magnitude. Even after considering an insulating SiO₂ layer, the computed electromagnetic field of the Ag@SiO₂ NPs leads to an averaged enhancement factor of ~6 at the LSPR wavelength (Figure 2b). Although the light concentration at the surface of the 10 nm SiO₂ layer is reduced with respect to the naked Ag NP, it can still support the non-radiative excitation of the nearby semiconductor (Figure 2c).

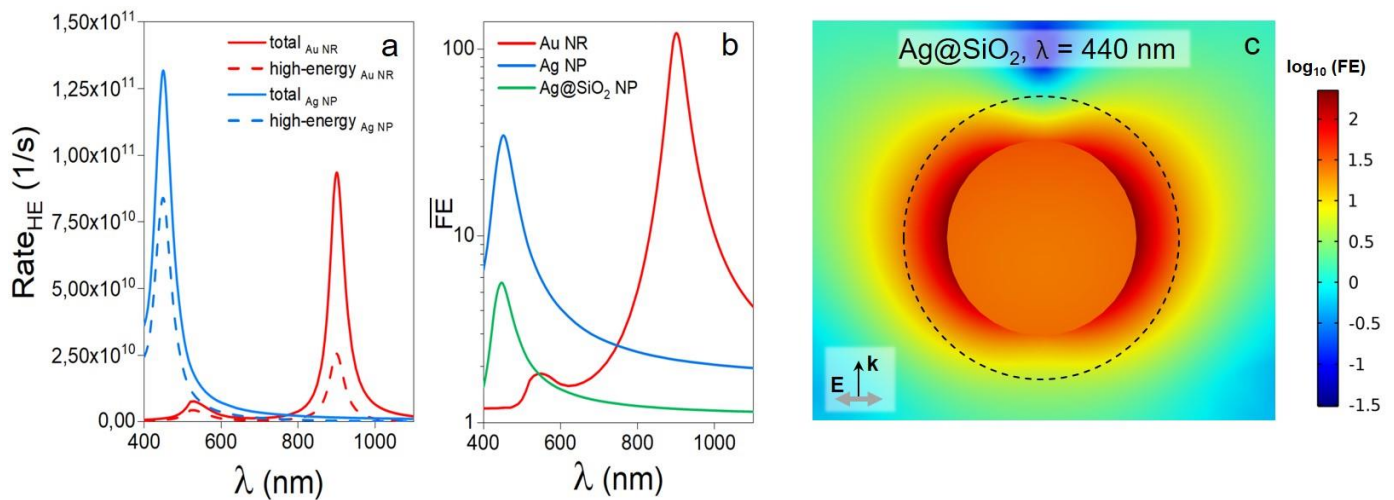


Figure 2. (a) Spectra of calculated rates of generation of hot electrons for both Au NRs and Ag NPs, in a homogenous dielectric medium simulating the environment with SiO₂ and TiO₂ in the hybrid. A second set of curves are included, indicating the rates of generation of high-energy hot electrons, or those with excess energies larger than the height of the Schottky barrier, taken in this calculation as $E_{\text{barrier}} = 1$ eV. (b) Spectra, in logarithmic scale, of the total field enhancement ($FE = |\mathbf{E}|^2/E_0^2$) around the plasmonic systems, calculated as an average value within a layer of 10 nm surrounding the nanostructures. (c) Color map of the FE (in logarithmic scale) for the Ag@SiO₂ NP. The black dashed line denotes the outer surface of the 10 nm SiO₂ coating, outside of which we can still observe regions where the enhancement surpasses 1 order of magnitude. Once the optimum amount of plasmonic photosensitizer has been established (100 nmol), we proceeded with the synthesis of new hybrids with a higher degree of complexity. In this case, multiple plasmonic components are included in the same material, thus leading to a new scenario in which HEI and PET pathways can be

combined rationally (Scheme 1). Moreover, the precise manipulation of the relative importance of both processes allows to create a model system in which their coexistence can be scrutinized. Along these lines, such a hybrid allows to understand the effect that the controlled integration of the PET mechanism will have in a system predominantly operated by a HEI-driven activation process that has already reached its maximum effective contribution (i.e., maximum metal concentration threshold).

In order to synthesize such material, we have reproduced the assembly process previously described with the difference that two plasmonic catalysts (100 nmol of metal of each one) are introduced in the same system. We have fabricated two complex hybrids with Au NRs and Ag NPs, the only difference between them being the surface functionalization of the latter (with or without an insulating SiO₂ layer). Scanning transmission electron microscopy (STEM) and energy-dispersive X-ray spectroscopy (EDX) characterization demonstrates again the homogeneous distribution of all inorganic materials (plasmonic components and TiO₂ NPs) onto the surface of the SiO₂ beads (Figure 3a, b). Moreover, EDX mapping helps to identify the homogeneous SiO₂ coating surrounding the Ag NPs in the second hybrid. The optical properties of both materials are very similar, with the main plasmonic contributions of Ag NPs and Au NRs clearly distinguishable. In this manner, the shoulder corresponding to Ag or Ag@SiO₂ NPs is located in the 420–430 nm range while the signature of Au NRs appears at ~890 nm (Figure 3c, d). When the two plasmonic components present a “naked” surface state (Figure 3a) HEI-based activation from both materials is the major contribution responsible for the photocatalytic activity, while PET activation from Ag plays a secondary role. However, when the Ag component is functionalized with a SiO₂ shell, it participates in the photoactivation by means of PET alone, making Au NRs the only HEI-operated component.

The catalytic activities of these complex hybrids have been analyzed once again using the photodegradation of RhB as a model reaction (Figure 3e). In this manner, we can compare their performances with respect to the reference hybrids containing a single plasmonic entity with 100 nmol of metal. The material composed by the combination of Au NRs and Ag NPs (without SiO₂ shell) shows a reduction in its catalytic activity (44% of degradation, grey column in Figure 3e) with respect to the systems in which Au NRs and Ag NPs are used independently (53% for each one). This difference can be explained as a result of the higher number of metal centers capable of capturing excited carriers in the TiO₂ which contribute effectively to faster recombination

kinetics in a photosensitization process. When Ag@SiO₂ NPs are added in combination with Au NRs, an important increase in the catalytic activity is observed (88% of degradation, black column in Figure 3e), matching the sum of both components when used separately (53% with the Au NRs and 33% for the Ag@SiO₂ NPs). This system surpasses substantially the value reached through a purely HEI-driven mechanism (53% for the system comprising Au NRs), highlighting the absence of a negative effect stemming from increasing the metal concentration beyond the maximum activity threshold found when using Au NRs alone (i.e., above the threshold for faster recombination kinetics). More importantly, this finding proves that a purely PET-driven mechanism can expand the photosensitization of a metal-semiconductor hybrid in which HEI has been optimized and reached its maximum activity.

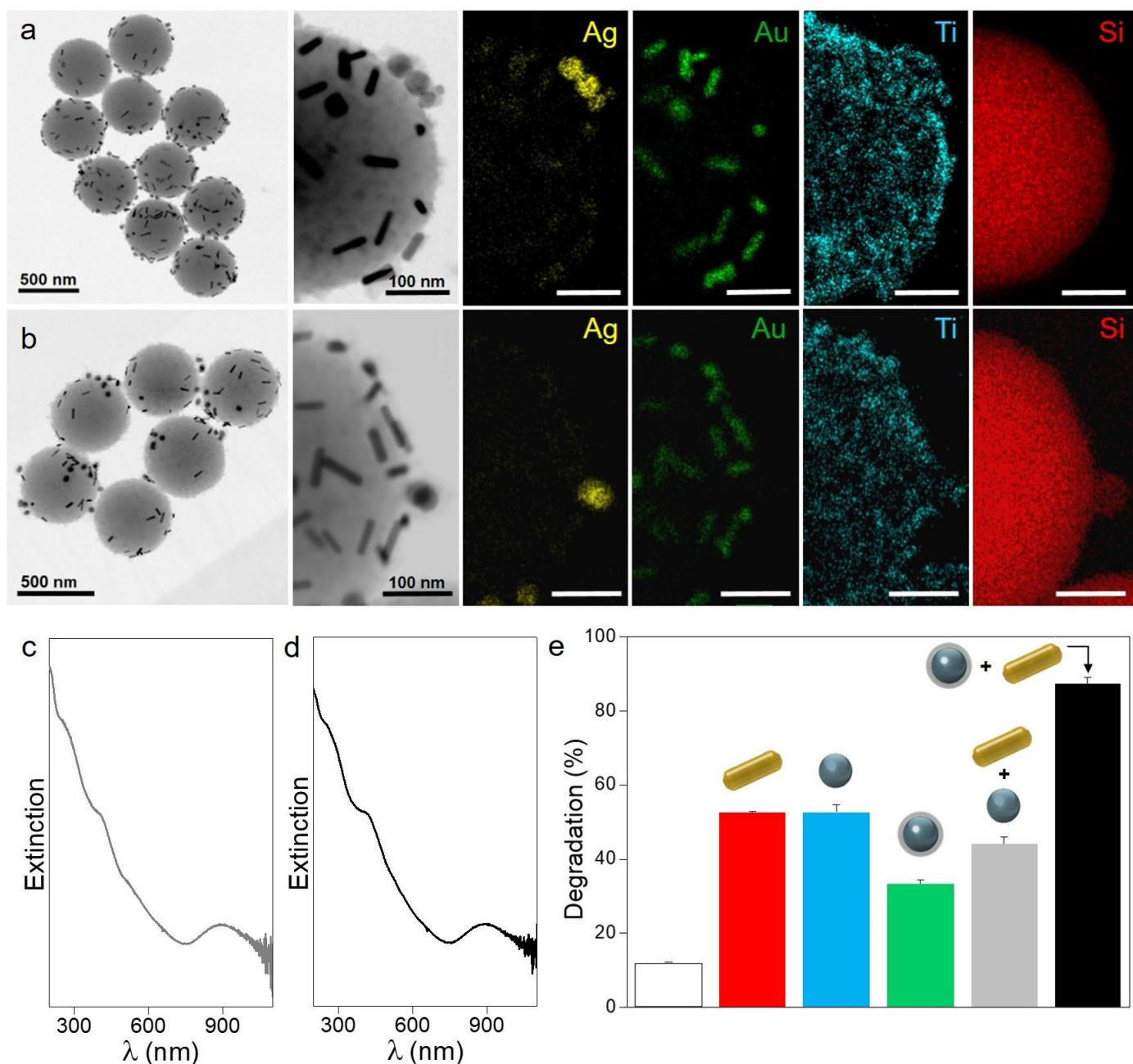


Figure 3. STEM images (bright field) and EDX mapping of the hybrid materials composed by (a) the assembly of Au NRs, Ag NPs and TiO₂ NPs and (b) by the assembly of Au NRs, Ag@SiO₂ NPs and TiO₂ NPs onto the SiO₂ beads. (c, d) Extinction spectra of the hybrid nanostructures based on Au NRs + Ag NPs and Au NRs + Ag@SiO₂ NPs, respectively. (e) Comparison of the photocatalytic activity of the different hybrids synthesized in the present work under 180 min of solar-simulated irradiation. Plasmonic components: 100 nmol of Ag NPs (blue), 100 nmol of Ag@SiO₂ NPs (green), 100 nmol of Au NRs (red), 100 nmol of Au NRs + 100 nmol of Ag NPs (grey); 100 nmol of Au NRs + 100 nmol of Ag@SiO₂ NPs (black). The white column in the left represents the reference sample with SiO₂ particles solely functionalized with TiO₂ NPs. All experiments have been performed at least three times (error bars are included).

We can go one step forward in the analysis of the catalytic activity of the complex hybrids containing two different plasmonic resonators by isolating the photoexcitation of each component, disentangling the performance of the different metals independently. In order to do so, two different glass-colored filters have been used to isolate different excitation ranges (400–700 nm targeting the resonance of the Ag components and 700–2400 nm targeting that of the Au NRs, since the only strong resonance of the latter lies in the NIR region) (Figure 4a, c). In the case of the Ag NPs in the complex Ag NP-Au NR nanohybrid an important reduction in the photocatalytic activity is observed with respect to the activation of the individual resonator with the entire solar spectrum (39% vs. 53%). A similar effect is observed when the Au NRs are excited with the NIR component (λ : 700–2400 nm), leading to a total degradation of 34% (Figure 4b). When the same experiment is run again with the hybrid nanostructures containing Au NRs and Ag@SiO₂ NPs we observe a similar trend (Figure 4c). In this case, when the visible component is used (400–700 nm) we observe that the original 33% photodegradation observed for Ag@SiO₂ NPs alone with the entire solar spectrum has been reduced to 23%. Similarly, the degree of degradation of RhB is reduced to 41% when only the NIR region (700–2400 nm) is used (Figure 4d). The partial decrease in photocatalytic activity with respect to the original values of the isolated plasmonic resonators can be explained by two major factors. Firstly, the photocatalytic activities obtained when using the optical filters are underestimated since their use induces a \sim 10% decrease in light transmittance (Figure S6a). Secondly, the use of the filters leads to the loss of the direct photoexcitation of TiO₂ from the UV segment of the solar simulator (12% degradation after 180 min). Besides these

experimental dissimilarities, the wavelength-dependent activation indicates that the hybrid photocatalysts allow for the selective activation of the plasmonic resonators, an operational feature with great potential when aiming at developing novel processes in wavelength-selective photochemistry or tandem photochemical reactions.

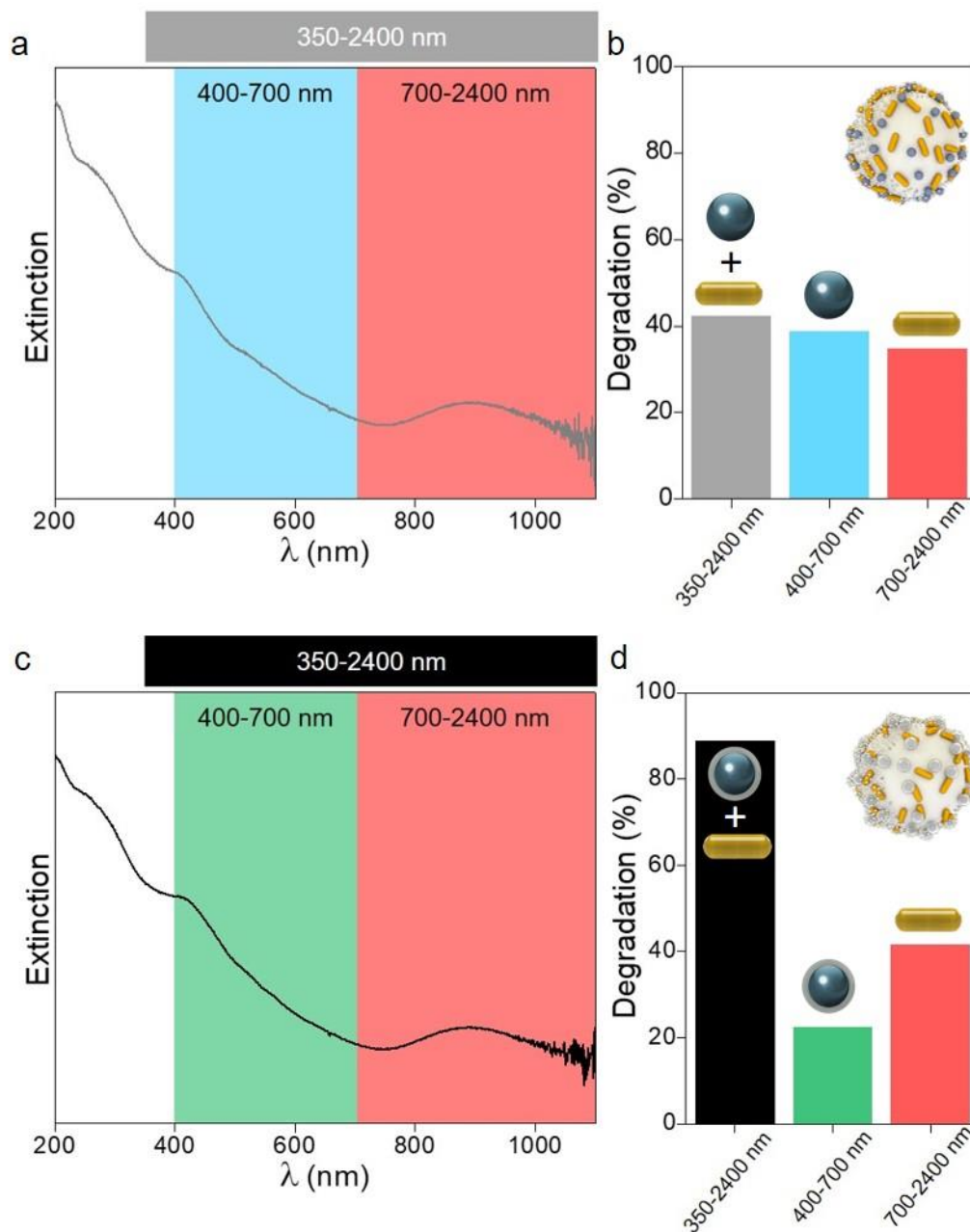


Figure 4. (a) Extinction spectra of the hybrid nanostructures containing Au NRs and Ag NPs and (b) their photocatalytic degradation capabilities of RhB with different excitation ranges. (c) Extinction spectra of the hybrids composed by the combination of Au NRs and Ag@SiO₂ NPs and their photocatalytic degradation capabilities of RhB with different excitation ranges.

Conclusions:

A layer-by-layer assembly protocol has been developed in order to produce complex photocatalytic hybrid nanostructures in which multiple plasmonic resonators are combined together with a large bandgap semiconductor. In this way, a distinctive scenario in which multiple photoactivation mechanisms are available in a single catalyst can be achieved. This approach allows the simultaneous operation of HEI and PET processes, producing an overall increase in the photocatalytic response of the system compared to that found when exploiting these mechanisms separately. The enhanced photosensitization of the semiconductor is the result of the simultaneous integration of both activation processes, overcoming current limitations in the use of hot charges in photochemical reactions. We believe that these results will contribute to a better understanding of the photocatalytic features of plasmonic metals, hence paving the way to the implementation of these materials as catalysts in a wide array of green and cost-effective chemical processes using sunlight as sole energy source.

Methods:

Materials: Tetrachloroauric acid ($\text{HAuCl}_4 \cdot 3\text{H}_2\text{O}$), hexadecyltrimethylammonium bromide (CTAB), sodium borohydride (NaBH_4), silver nitrate (AgNO_3), hydrochloric acid (HCl), L-ascorbic acid (AA), poly(allylamine hydrochloride) (PAH, MW: 17500 g/mol), sodium chloride (NaCl), poly(styrenesulfonate) (PSS, MW: 14900 g/mol), tannic acid (TA), tetraethylorthosilicate 98% (TEOS), ammonium hydroxide solution 28–30% (NH_4OH) and sodium citrate ($\text{Na}_3\text{C}_6\text{H}_5\text{O}_7$), were purchased from Sigma-Aldrich. TiO_2 nanoparticles of 5 nm were purchased from Nanoamor. Pure grade ethanol and Milli-Q grade water were used in all preparations.

Synthesis and functionalization of SiO_2 beads: Monodisperse SiO_2 spheres (501 (± 1) nm) were prepared using a modified Stöber method.⁵⁰ Typically, a TEOS solution (1.7 mL, 1.2 M) was added to a solution containing ethanol (18.12 mL), ammonium hydroxide (1.96 mL), and water (3.21 mL). This mixture was stirred at room temperature for 2 h. The excess of reagents was removed by three centrifugation-redispersion cycles with ethanol (2800 g, 20 min).

Subsequently, PAH was dissolved in a 0.5 M NaCl aqueous solution (pH 5.0) with a final polymer concentration of 1 mg/mL. Then, 25 mL of the positively charged PAH solution were added to the SiO_2 NPs

(20 mg) and stirred at room temperature for 30 min. The excess of reagents was removed by three centrifugation-redispersion cycles with water (4000 g, 20 min).

Synthesis of Au NRs and PSS coating: AuNRs with localized surface plasmon resonance (LSPR) centered at 818 nm were synthesized by the seed-mediated growth method as described elsewhere.⁵¹ The dimensions obtained from TEM were 53.8 (± 4.1) nm of length and 13.3 (± 1.1) nm of thickness (aspect ratio 4.05). Au NRs were subsequently coated with a layer of a negatively charged polyelectrolyte (PSS) in order to proceed to the deposition onto the positively charged PAH functionalized silica beads.⁵²

Synthesis of Ag NPs and SiO₂ coating: Ag NPs were synthesized as described elsewhere.⁵³ The size was fixed at 42.7 \pm 3.4 nm by adjusting the concentration of AgNO₃, Na₃C₆H₅O₇ and TA to 1 mM, 2.45 mM and 0.2 mM, respectively. The Ag NPs were subsequently coated with a thin layer of silica (10.0 \pm 0.5 nm) by following a previously published procedure.⁵⁴

Adsorption of AuNRs@PSS, Ag NPs and AgNPs@SiO₂ onto functionalized SiO₂ beads. The solution of NPs (0.5, 1 and 2 mL of AuNRs@PSS 0.5 mM; 0.21, 0.42 and 0.84 mL of AgNPs 1.19 mM; 0.5, 1 and 2 mL of AgNPs@SiO₂ 0.5 mM) were added to 5 mg of functionalized silica NPs (50, 100 and 200 nmol of metal per mg of SiO₂ in all cases). The mixture was stirred at room temperature for 3 h and washed by three centrifugation-redispersion cycles (4000 g, 20 min). The product was redispersed in 5 mL of water.

Assembly of Ag NPs and AgNPs@SiO₂ onto SiO₂@AuNRs. 0.42 mL of Ag NPs 1.19 mM and 1 mL of AgNPs@SiO₂ 0.5 mM were added to 5 mg of SiO₂@AuNRs (100 nmol of Au per mg of SiO₂) functionalized with PAH. The samples were stirred for 3 h and washed by three centrifugation-redispersion cycles with water (4000 g, 20 min). Finally, each product was redispersed in 5 mL of water.

Deposition of TiO₂. 50 mg of TiO₂ (5 nm) redispersed in 100 mL of a sodium citrate solution (2,5 mM) was sonicated for 1 h with an ultrasonic tip. The aggregates of TiO₂ NPs were removed by centrifugation (1340 g, 10 min). Then, 5 mL of the SiO₂@NPs solution coated with another layer of PAH was added to 4 mL of the solution of TiO₂ and stirred at room temperature for 60 min. The excess of TiO₂ was removed by three centrifugation-redispersion cycles (4000 g, 20 min). Finally, the product was redispersed in 5 mL of water. The ratio TiO₂/SiO₂ was 2.1 \pm 0.1 wt% (ICP analysis).

Chemical, structural and optical characterization: TEM images were obtained using a JEOL JEM 1010 transmission electron microscope operating at an acceleration voltage of 100 kV. STEM images (Bright Field detector) and EDX maps were obtained in a probe-corrected FEI ChemiSTEM electron microscope operating at 200 kV. UV-visible-NIR spectra were obtained with Hewlett-Packard HP8453 and Cary 5000 spectrophotometers.

Photocatalytic Study: The photocatalytic activity of the hybrids was evaluated by the degradation of rhodamine B (RhB) in an aqueous solution inside a controlled water bath at 25 °C for 180 min under light irradiation from a LOT solar simulator (300 W Xe lamp) with $\lambda = 350\text{--}2400$ nm. The solutions were prepared mixing 200 μL of an aqueous solution of RhB (1 mM), 4 mL of the hybrid solution (1 mg/mL) and 15.8 mL of Milli-Q water. The mixtures were stirred for 1 h in the dark to blend well and allow the adsorption-desorption equilibrium before the irradiation. Aliquots of 2.5 mL were taken with intervals of 30 min during the experiments in order to measure the variation in the absorbance. When necessary, a glass colored filter was introduced in the solar simulator (filter FM201 with $\lambda = 400\text{--}700$ nm and 90% of transmittance, to evaluate the photocatalytic activity in the visible region of the spectrum; filter 700FH 90 with $\lambda = 700\text{--}1100$ nm and 90% of transmittance, to evaluate the photocatalytic activity in the NIR region of the spectrum) (Figure S6).

Theoretical methods. The simulations obtained the optical response of the plasmonic systems within a classical electrodynamics framework, numerically solved using finite element methods (FEM) as implemented by the COMSOL commercial software package. The models of the NPs had sizes chosen in accord with the average ensemble sizes in the experiment (Figure S1) and with their optical profiles (Figure 1). The models for the nanorods are 53 nm \times 13 nm in size, while the Ag NPs are 45 nm in diameter, and their external SiO₂ coating has a thickness of 10 nm. The complex permittivity of Au and Ag were extracted from published experimental datasets.^{55,56} The refractive index of the medium was taken as either that of water ($n_w=1.33$), or a weighted average of the materials surrounding the plasmonic systems in the hybrids (resulting in $n_{\text{hybrids}}\approx 1.5$). An incidence intensity of $3.6\cdot 10^3$ W/cm² was assumed in the calculations. The field enhancement (FE) magnitude that is presented in the main text is defined as $E = |\mathbf{E}|^2/E_0^2$, where E_0 is the electric field's amplitude of the incoming radiation. The rates of generation of intraband hot carriers were

calculated using a quantum formalism that accounts for the effect of the surface of the NPs, critical for allowing the excitation of high-energy hot carriers without violating the conservation of linear momentum. Full description of this formalism can be found in previous publications.^{28,47,57}

Additional information

TEM characterization; photochemical tests and control experiments; theoretical extinction and scattering cross-sections and field distributions of the plasmonic resonators.

Author information

Corresponding authors

*E-mail: govorov@ohiou.edu

*E-mail: miguel.comesana-hermo@u-paris.fr

*E-mail: macorrea@uvigo.es

ORCID

Yoel Negrín-Montecelo: 0000-0002-0977-7014

Xiang-Tian Kong: 0000-0002-8554-0369

Lucas V. Besteiro: 0000-0001-7356-7719

Enrique Carbó-Argibay: 0000-0001-7472-9564

Zhiming M. Wang: 0000-0003-2945-4834

Moisés Pérez-Lorenzo: 0000-0002-7157-5966

Alexander O. Govorov: 0000-0003-1316-6758

Miguel Comesaña-Hermo: 0000-0001-8471-5510

Miguel A. Correa-Duarte: 0000-0003-1950-1414

Notes

The authors declare no competing financial interest.

Acknowledgments

This work was funded by Ministerio de Economía y Competitividad de España (CTM2017-84050-R), Xunta de Galicia (Centro Singular de Investigación de Galicia - Accreditation 2019-2022 ED431G 2019/06 and IN607A 2018/5), and European Union-ERDF (Interreg V-A - Spain-Portugal 0245_IBEROS_1_E, 0712_ACUINANO_1_E, and 0624_2IQBIONEURO_6_E, and Interreg Atlantic Area NANOCULTURE 1.102.531). M.C.-H. thanks CNRS for support. L.V.B. acknowledges support from the National Natural Science Foundation of China (Project No. 12050410252). A.O.G thanks the Nanoscale & Quantum Phenomena Institute at Ohio University for its support.

Bibliography:

1. Tagliabue, G. *et al.* Ultrafast hot-hole injection modifies hot-electron dynamics in Au/p-GaN heterostructures. *Nat. Mater.* **19**, 1312–1318 (2020).
2. Tagliabue, G. *et al.* Quantifying the role of surface plasmon excitation and hot carrier transport in plasmonic devices. *Nat. Commun.* **9**, 3394 (2018).
3. Yu, S., Wilson, A. J., Heo, J. & Jain, P. K. Plasmonic Control of Multi-Electron Transfer and C-C Coupling in Visible-Light-Driven CO₂ Reduction on Au Nanoparticles. *Nano Lett.* **18**, 2189–2194 (2018).
4. Wilson, A. J. & Jain, P. K. Light-Induced Voltages in Catalysis by Plasmonic Nanostructures. *Acc. Chem. Res.* **53**, 1773–1781 (2020).
5. Aslam, U., Rao, V. G., Chavez, S. & Linic, S. Catalytic conversion of solar to chemical energy on plasmonic metal nanostructures. *Nat. Catal.* **1**, 656–665 (2018).
6. Linic, S., Chavez, S. & Elias, R. Flow and extraction of energy and charge carriers in hybrid plasmonic nanostructures. *Nat. Mater.* **15**, (2021).
7. Lee, S. H. *et al.* Direct Observation of Plasmon-Induced Interfacial Charge Separation in Metal/Semiconductor Hybrid Nanostructures by Measuring Surface Potentials. *Nano Lett.* **18**, 109–116 (2018).

8. Jang, Y. H. *et al.* Plasmonic Solar Cells: From Rational Design to Mechanism Overview. *Chem. Rev.* **116**, 14982–15034 (2016).
9. Atwater, H. A. & Polman, A. Plasmonics for improved photovoltaic devices. *Nat. Mater.* **9**, 205–213 (2010).
10. Linic, S., Christopher, P. & Ingram, D. B. Plasmonic-metal nanostructures for efficient conversion of solar to chemical energy. *Nat. Mater.* **10**, 911–921 (2011).
11. Zhang, X. *et al.* Product selectivity in plasmonic photocatalysis for carbon dioxide hydrogenation. *Nat. Commun.* **8**, 14542 (2017).
12. Liu, J. *et al.* Metal@semiconductor core-shell nanocrystals with atomically organized interfaces for efficient hot electron-mediated photocatalysis. *Nano Energy* **48**, 44–52 (2018).
13. Mubeen, S. *et al.* An autonomous photosynthetic device in which all charge carriers derive from surface plasmons. *Nat. Nanotechnol.* **8**, 247–51 (2013).
14. Liz-Marzán, L. M. Tailoring Surface Plasmons through the Morphology and Assembly of Metal Nanoparticles. *Langmuir* **22**, 32–41 (2006).
15. Jain, P. K., Lee, K. S., El-Sayed, I. H. & El-Sayed, M. A. Calculated absorption and scattering properties of gold nanoparticles of different size, shape, and composition: Applications in biological imaging and biomedicine. *J. Phys. Chem. B* **110**, 7238–7248 (2006).
16. Langer, J. *et al.* Present and Future of Surface-Enhanced Raman Scattering. *ACS Nano* **14**, 28–117 (2020).
17. Zhang, Y. *et al.* Surface-Plasmon-Driven Hot Electron Photochemistry. *Chem. Rev.* **118**, 2927–2954 (2018).
18. Hartland, G. V., Besteiro, L. V., Johns, P. & Govorov, A. O. What's so Hot about Electrons in Metal Nanoparticles? *ACS Energy Lett.* **2**, 1641–1653 (2017).
19. Zhou, L. *et al.* Quantifying hot carrier and thermal contributions in plasmonic photocatalysis. *Science* **362**, 69–72 (2018).

20. Ingram, D. B. & Linic, S. Water splitting on composite plasmonic-metal/semiconductor photoelectrodes: Evidence for selective plasmon-induced formation of charge carriers near the semiconductor surface. *J. Am. Chem. Soc.* **133**, 5202–5205 (2011).
21. Rao, V. G., Aslam, U. & Linic, S. Chemical Requirement for Extracting Energetic Charge Carriers from Plasmonic Metal Nanoparticles to Perform Electron-Transfer Reactions. *J. Am. Chem. Soc.* **141**, 643–647 (2018).
22. Cushing, S. K. *et al.* Tunable Nonthermal Distribution of Hot Electrons in a Semiconductor Injected from a Plasmonic Gold Nanostructure. *ACS Nano* **12**, 7117–7126 (2018).
23. Saavedra, J. R. M., Asenjo-Garcia, A. & García de Abajo, F. J. Hot-Electron Dynamics and Thermalization in Small Metallic Nanoparticles. *ACS Photonics* **3**, 1637–1646 (2016).
24. Pensa, E. *et al.* Spectral Screening of the Energy of Hot Holes over a Particle Plasmon Resonance. *Nano Lett.* **19**, 1867–1874 (2019).
25. Tatsuma, T., Nishi, H. & Ishida, T. Plasmon-induced charge separation: chemistry and wide applications. *Chem. Sci.* **8**, 3325–3337 (2017).
26. Chang, L. *et al.* Electronic Structure of the Plasmons in Metal Nanocrystals: Fundamental Limitations for the Energy Efficiency of Hot Electron Generation. *ACS Energy Lett.* **4**, 2552–2568 (2019).
27. Bumajdad, A. & Madkour, M. Understanding the superior photocatalytic activity of noble metals modified titania under UV and visible light irradiation. *Phys. Chem. Chem. Phys.* **16**, 7146–58 (2014).
28. Sousa-Castillo, A. *et al.* Boosting Hot Electron-Driven Photocatalysis through Anisotropic Plasmonic Nanoparticles with Hot Spots in Au–TiO₂ Nanoarchitectures. *J. Phys. Chem. C* **120**, 11690–11699 (2016).
29. Sakthivel, S. *et al.* Enhancement of photocatalytic activity by metal deposition: Characterisation and photonic efficiency of Pt, Au and Pd deposited on TiO₂ catalyst. *Water Res.* **38**, 3001–3008 (2004).
30. Asapu, R. *et al.* Electron Transfer and Near-Field Mechanisms in Plasmonic Gold-Nanoparticle-Modified TiO₂ Photocatalytic Systems. *ACS Appl. Nano Mater.* **2**, 4067–4074 (2019).

31. Li, J. *et al.* Plasmon-induced resonance energy transfer for solar energy conversion. *Nat Phot.* **9**, 601–607 (2015).
32. Cushing, S. K. *et al.* Photocatalytic Activity Enhanced by Plasmonic Resonant Energy Transfer from Metal to Semiconductor. *J. Am. Chem. Soc.* **134**, 15033–15041 (2012).
33. Zhan, C., Chen, X. J., Huang, Y. F., Wu, D. Y. & Tian, Z. Q. Plasmon-Mediated Chemical Reactions on Nanostructures Unveiled by Surface-Enhanced Raman Spectroscopy. *Acc. Chem. Res.* **52**, 2784–2792 (2019).
34. Kamarudheen, R., Aalbers, G. J. W., Hamans, R. F., Kamp, L. P. J. & Baldi, A. Distinguishing among All Possible Activation Mechanisms of a Plasmon-Driven Chemical Reaction. *ACS Energy Lett.* **5**, 2605–2613 (2020).
35. Kamarudheen, R., Castellanos, G. W., Kamp, L. P. J., Clercx, H. J. H. & Baldi, A. Quantifying Photothermal and Hot Charge Carrier Effects in Plasmon-Driven Nanoparticle Syntheses. *ACS Nano* **12**, 8447–8455 (2018).
36. Wu, N. Plasmonic metal-semiconductor photocatalysts and photoelectrochemical cells: A review. *Nanoscale* **10**, 2679–2696 (2018).
37. Negrín-Montecelo, Y. *et al.* Photophysical Effects behind the Efficiency of Hot Electron Injection in Plasmon-Assisted Catalysis: The Joint Role of Morphology and Composition. *ACS Energy Lett.* **5**, 395–402 (2020).
38. Cushing, S. K. & Wu, N. Progress and Perspectives of Plasmon-Enhanced Solar Energy Conversion. *J. Phys. Chem. Lett.* **7**, 666–675 (2016).
39. Cushing, S. K. *et al.* Controlling Plasmon-Induced Resonance Energy Transfer and Hot Electron Injection Processes in Metal@TiO₂ Core-Shell Nanoparticles. *J. Phys. Chem. C* **119**, 16239–16244 (2015).
40. You, X., Ramakrishna, S. & Seideman, T. Unified theory of plasmon-induced resonance energy transfer and hot electron injection processes for enhanced photocurrent efficiency. *J. Chem. Phys.*

- 149**, 174304 (2018).
41. Caruso, F., Caruso, R. A. & Möhwald, H. Nanoengineering of inorganic and hybrid hollow spheres by colloidal templating. *Science* **282**, 1111–1114 (1998).
 42. Sousa-Castillo, A. *et al.* Remote Activation of Hollow Nanoreactors for Heterogeneous Photocatalysis in Biorelevant Media. *Nano Lett.* **20**, 7068–7076 (2020).
 43. Baffou, G., Bordacchini, I., Baldi, A. & Quidant, R. Simple experimental procedures to distinguish photothermal from hot-carrier processes in plasmonics. *Light Sci. Appl.* **9**, 108 (2020).
 44. Mascaretti, L. & Naldoni, A. Hot electron and thermal effects in plasmonic photocatalysis. *J. Appl. Phys.* **128**, 041101 (2020).
 45. Rej, S. *et al.* Determining Plasmonic Hot Electrons and Photothermal Effects during H₂ Evolution with TiN–Pt Nanohybrids. *ACS Catal.* **10**, 5261–5271 (2020).
 46. Brown, A. M., Sundararaman, R., Narang, P., Goddard, W. A. & Atwater, H. A. Nonradiative plasmon decay and hot carrier dynamics: Effects of phonons, surfaces, and geometry. *ACS Nano* **10**, 957–966 (2016).
 47. Santiago, E. Y. *et al.* Efficiency of Hot-Electron Generation in Plasmonic Nanocrystals with Complex Shapes: Surface-Induced Scattering, Hot Spots, and Interband Transitions. *ACS Photonics* **7**, 2807–2824 (2020).
 48. Szydło, N. & Poirier, R. I–V and C–V Characteristics of Au/TiO₂ Schottky diodes. *J. Appl. Phys.* **51**, 3310–3312 (1980).
 49. Chinnamuthu, P., Dhar, J. C., Mondal, A., Bhattacharyya, A. & Singh, N. K. Ultraviolet detection using TiO₂ nanowire array with Ag Schottky contact. *J. Phys. D: Appl. Phys.* **45**, 135102 (2012).
 50. Stöber, W., Fink, A. & Bohn, E. Controlled Growth of Monodisperse Silica Spheres in the Micron Size Range. *J. Colloid Interface Sci.* **26**, 62–69 (1968).
 51. Scarabelli, L., Sánchez-Iglesias, A., Pérez-Juste, J. & Liz-Marzán, L. M. A “Tips and Tricks” Practical Guide to the Synthesis of Gold Nanorods. *J. Phys. Chem. Lett.* **6**, 4270–4279 (2015).

52. Pastoriza-Santos, I., Pérez-Juste, J. & Liz-Marzán, L. M. Silica-Coating and Hydrophobation of CTAB-Stabilized Gold Nanorods. *Chem. Mater.* **18**, 2465–2467 (2006).
53. Bastús, N. G., Merkoçi, F., Piella, J. & Puntès, V. Synthesis of Highly Monodisperse Citrate-Stabilized Silver Nanoparticles of up to 200 nm: Kinetic Control and Catalytic Properties. *Chem. Mater.* **26**, 2836–2846 (2014).
54. Fernández-López, C. *et al.* Highly Controlled Silica Coating of PEG-Capped Metal Nanoparticles and Preparation of SERS-Encoded Particles. *Langmuir* **25**, 13894–13899 (2009).
55. Johnson, P. B. & Christy, R. W. Optical Constants of the Noble Metals. *Phys. Rev. B* **6**, 4370–4379 (1972).
56. Palik, E. D. *Handbook of Optical Constants of Solids (Volume 2)*. (Academic Press Inc., 1991).
57. Besteiro, L. V., Kong, X.-T., Wang, Z., Hartland, G. & Govorov, A. O. Understanding Hot-Electron Generation and Plasmon Relaxation in Metal Nanocrystals: Quantum and Classical Mechanisms. *ACS Photonics* **4**, 2759–2781 (2017).